

Global median filtering forensic method based on Pearson parameter statistics

ISSN 1751-9659

Received on 22nd August 2018

Revised 1st March 2019

Accepted on 18th March 2019

E-First on 23rd August 2019

doi: 10.1049/iet-ipr.2018.6074

www.ietdl.org

Abhinav Gupta¹ , Divya Singhal¹¹Department of Electronics and Communication Engineering, Jaypee Institute of Information Technology, A-10, Sector-62, Noida, UP 201301, India E-mail: abhinav.gupta@jiit.ac.in

Abstract: Median filtering forensics in images is a subject under intense study nowadays. Existing median filtering detectors are developed based on hand-crafted features and convolutional neural networks (CNN). Among hand-crafted features based detectors, most of the detector's performance deteriorate for low-resolution images compressed with low-quality factors. However, CNN-based detectors are found to be more robust at the expense of large database and large training time requirement. In this study, the authors propose a robust median filtering detector by exploiting the statistics of the Pearson parameter κ . κ is defined as the polynomial ratio of skewness and kurtosis. To capture fingerprints of median filtering, κ is determined for the median filtered residual (MFR) of the images to construct a novel feature set of 23 dimensions. The efficacy of the proposed feature set, against existing hand-crafted features based and CNN-based detectors, is established by a series of experiments for global median filtering detection. Results reveal that the proposed feature set exhibits performance gain of 2–4% against existing hand-crafted features based detectors and an approximate gain of 4% against CNN-based detector for detection of low-resolution median filtered images compressed with low-quality factors.

1 Introduction

The digitisation of images and multimedia facilitates its easy handling and usage along with ease of tampering it. Thus, it becomes important to verify the genuineness of media or images before further circulating or making a conclusion based on it. As a result, many researchers are motivated towards the field of digital image forensics to determine the processing history of an image. In recent years, researchers have focused on developing forensic methods for blind image authentication based on the fact that forgeries may not change the visual appearance of images but may significantly alter the underlying statistical properties of the test image [1]. These statistical properties are known as intrinsic fingerprints of the forgery performed on the images. In recent works, intrinsic fingerprints have been extracted in terms of hand-crafted features and convolutional neural network (CNN)-based features. Hand-crafted features based detectors are mainly developed for detection of image resampling [2], JPEG compression [3], contrast enhancement [4, 5], median filtering [6–17] and multiple manipulations [18]. However, recent CNN-based detectors have focused on median filtering detection [19, 20] and multiple manipulation detections [21, 22]. Apart from forensic detectors, researchers have also focused on developing anti-forensic detectors [23, 24] to improve the performance of forensic detectors.

Median filtering, being a non-linear rank-order filter with edge preservation property, is mostly used for the removal of noise and outlier pixel values from images without blurring the image. Its edge preservation property may be misused by an offender for hiding underlying content-changing manipulations to create visually realistic images. Also, median filtering has been used as an anti-forensic tool to conceal the fingerprints of re-sampling [25] and compression [26]. The above facts have motivated us to develop a scheme for median filtering detection to verify the trustworthiness of the image under question. In this paper, a 23-dimensional novel feature set based on a histogram of Pearson parameter and its statistical features is proposed. Proposed feature set is comprehensively evaluated on five different databases (UCID [27], BOWS2 [28], BOSSBase [29], RAISE [30] and NRCS [31]) to assess its benefits and limitations. The proposed feature set is

compared with hand-crafted features-based detectors MFF [6], AR [7], MFD [10], SK/SKR [32] and CNN-based detector [19]. The contribution of proposed work is three-fold: (i) analysis of distinct residual value blocks in the original image MFR and median filtered image MFR, (ii) low-dimensional feature set construction for median filtering forensics and (iii) robustness of the proposed detector under different test case scenarios with significant advantages over state-of-the-art methods, especially under no compression and JPEG compression with very low quality factors.

The remaining of the paper is organised as follows. Section 2 describes the related work done in the field. New feature set construction with a detailed analysis of motivation for this work and Pearson parameter κ -based intrinsic fingerprints for median filtering detection are discussed in Section 3. Section 4 discusses the experimental setup and databases used in this study. Section 5 shows the detailed experimental performance of the proposed feature set. Section 6 concludes the paper.

2 Literature review

2.1 Median filter

Two-dimensional non-linear median filter replaces the central pixel value with the median of all pixel values in the neighbourhood window of size $s \times s$. For images, s normally takes odd values ($s = 3, 5, 7, \dots$). In this work, the most common median filtering window sizes $s = 3$ and $s = 5$ are considered. For a particular pixel with value $p(m, n)$ at the position (m, n) in an image, the corresponding pixel after median filtering with window size $s \times s$, $p_s(m, n)$ can be written as

$$p_s(m, n) = \text{median}_s[p(i, j)] \quad (1)$$

where

$$i \in \left(m - \frac{s-1}{2}, \dots, m + \frac{s-1}{2} \right)$$

$$j \in \left(n - \frac{s-1}{2}, \dots, n + \frac{s-1}{2} \right)$$

and

$$m, n, i, j \in \mathbb{Z}$$

Here $\text{median}_s[\cdot]$ denotes median operator which operates by first ranking grey levels of window size $s \times s$ in ascending order and then selecting the middle grey level among them.

2.2 Median filtering detection

Bovik [33] analysed non-linear median filtering operation and proposed a quantitative measure in terms of non-zero probability of equal median filtered values from sliding windows. This effect is termed as streaking effect and utilised by many researchers to develop distinct hand-crafted features for median filtering forensics. Kirchner and Fridrich [13] have utilised streaking artefacts and proposed a ratio $\rho = h_0/h_i$ to capture median filtering fingerprints in first-order difference images. Here, h_i denotes the count of i in first-order difference image. For median filtered images, $\rho \gg 1$ is expected to be true in light of the streaking effect. However, under JPEG post-compression, ratio ρ fails to detect median filtering. Kirchner and Fridrich [13] demonstrated the efficacy of subtractive pixel adjacency matrix (*SPAM*) [34] features and exploited this large feature set (686 features) for median filtering detection under post JPEG compression with high to moderate quality factors. Another median filtering detection method utilising streaking effect is proposed by Cao *et al.* [12] which focuses on the probability of zero in textured regions of first-order difference images. However, this method effectively detects median filtering in uncompressed form, but performance is degraded under the attack of JPEG compression.

Further, Yuan [6] exploits the relationships among different pixels of a small window and extracted 44-dimensional feature set named as median filtering forensics (*MFFs*). However, *MFF* performs almost perfect classification in uncompressed form but suffers significant performance loss under the attack of JPEG post compression. Chen *et al.* [11] utilised cumulative distribution function of first and second-order difference images and the joint distribution of adjacent difference pairs to construct a 56-dimensional feature set for median filtering forensics. This method achieves good detection accuracy for JPEG compressed low-resolution images at the cost of a large feature set.

Kang *et al.* [7] demonstrated the effectiveness of median filtered residual (*MFR*) over first-order pixel difference, direct pixel intensities and exploited it to construct 10-dimensional feature set based on auto-regressive (*AR*) model coefficients. This method has proven to be robust for median filtering detection under JPEG compression at high to moderate quality factors, but its performance is degraded under low-quality factors of compression and uncompressed form.

Recently, Rhee [10] has captured the variations in neighbouring pixel pairs in spatial and frequency domains to construct 19-dimensional feature set termed as median filtering detection (*MFD*). Experimental results show that detector *MFD* achieves comparable performance with the relatively small dimensional feature set. Further, Yang *et al.* [8] proposed an 81-dimensional robust median filtering forensics detector based on MFRs, average filtered residuals and Gaussian filtered residuals of the image under question. This method has achieved good accuracy compared to previous detectors with a trade-off between accuracy and feature set dimensions. Niu *et al.* [14] proposed the 128-dimensional feature set based on rotation invariant local binary patterns and pixel difference matrix. Results indicate that this detector achieves good detection accuracy under low-quality JPEG compression at the cost of large feature set dimensions.

Further, to reduce feature set dimensionality along with robust detection, Liu *et al.* [15] proposed a 20-dimensional frequency domain feature set named as annular accumulated points.

Experimental results show that the proposed detector is robust for a combination of low-resolution and moderate JPEG quality factors. In a recent work [17], image discrete cosine transform (DCT) sub-band coefficients are utilised as fingerprints for median filtering detection. The method works well for low-resolution images with a large feature set of variable length, which varies according to the image size. In another work [32], statistics of skewness and kurtosis have been exploited to construct 19-dimensional feature set *SK*. The feature set is constructed based on the analysis of two grey value blocks (block size 3×3) in original and median filtered images. Results prove its efficacy in uncompressed form and in some novel test case scenarios, whereas performance is deteriorated for low-resolution images with post JPEG compression. Thus, to maintain the robustness of method for post JPEG compression, the authors in [32] have proposed novel residual-based feature set *SK_R*.

Along with hand-crafted features-based detectors, CNN-based detectors are also gaining popularity nowadays. CNN extracts the low-level features directly from the images, thus improve the detection accuracy as compared to hand-crafted features-based detectors. In [19], MFR of an image is fed into CNN to detect median filtering in images. Results show good detection accuracy for low-resolution images. In another CNN-based detector [20], the input image is interpolated and cropped before feeding it into CNN. It has been found that the detector is robust for median filtering detection in low-resolution images. However, the good detection accuracies by CNN-based detectors are achieved at the cost of massive training database and large training time. In light of the recent works discussed above, we found that there is still a requirement of a novel detector enriched with positive aspects of hand-crafted features-based detectors (low feature set dimensions and less training time) and CNN-based detectors (high accuracy).

3 New feature set construction

3.1 Pearson parameter κ

In previous works, the Pearson system of distributions [35] has been exploited for a variety of applications [36–42]. In the field of wireless communication, type IV Pearson distributions have been exploited to approximate sum and linear combinations of lognormal random variables [36–38]. Pearson distributions have been utilised for grey level characterisation [39] in ultrasound imaging and speckle characterisation [40] in echocardiographic images. Also, Pearson distributions have been used for speckle modelling in SAR images [41] and colour object tracking [42]. A Pearson system of distributions is characterised by the parameter κ which is defined as the polynomial ratio of skewness and kurtosis. In this work, the parameter κ is explored for a novel application in the field of median filtering forensics. A brief derivation of the parameter κ in terms of skewness and kurtosis is discussed for better understanding.

An appropriate method for generation of unimodal probability distributions can be achieved by solving the differential equation [35]

$$\frac{1}{g(x)} \frac{dg(x)}{dx} = \frac{x+a}{c_0 + c_1x + c_2x^2} \quad (2)$$

where $g(x)$ is the probability density function (pdf) and a, c_0, c_1 and c_2 are constant parameters.

The constant parameters a, c_0, c_1 and c_2 can be obtained in terms of skewness (S) and kurtosis (K). After that, (2) can be rewritten as (see (3)). Here $S=\mu_3/\mu_2^{3/2}$ and $K=\mu_4/\mu_2^2$. μ_2, μ_3 and μ_4 are second, third and fourth centralised moments, respectively. The detailed solution regarding the transition of (2) into (3) can be seen in [35, 39]. The nature of the roots of $c_0 + c_1x + c_2x^2$ (denominator of (2)) is determined by the discriminant function $c_1^2 - 4c_0c_2 \leq 0$, which

$$\frac{1}{g(x)} \frac{dg(x)}{dx} = - \frac{x + ((\sqrt{\mu_2}S(K+3))/2(5K-6S^2-9))}{((2K-3S^2-6)x^2 + \sqrt{\mu_2}S(K+3)x + \mu_2(4K-3S^2))/2(5K-6S^2-9)} \quad (3)$$

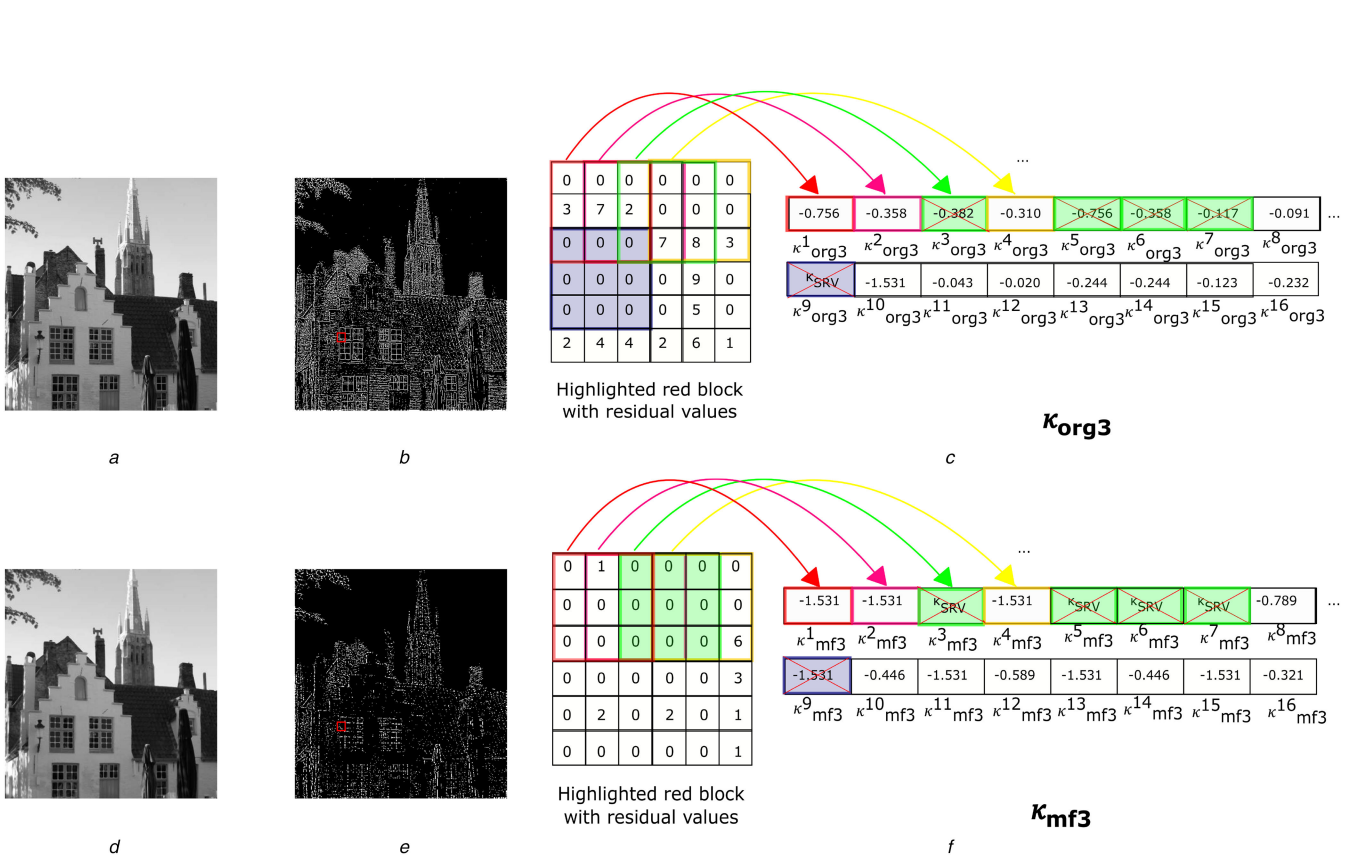


Fig. 1 κ vector construction method from original and corresponding median filtered image MFR

- (a) Original image from BOWS2 [28] database,
- (b) MFR of Fig. 1a,
- (c) κ vector formation from an example block of Fig. 1b,
- (d) Median filtered image with window size 3×3 ,
- (e) MFR of Fig. 1d,
- (f) κ vector formation from an example block of Fig. 1e. For better visualisation, original image MFR and median filtered image MFR are displayed log compressed

can be rewritten as $c_1^2/4c_0c_2 \leq 1$. Pearson defined $\kappa = c_1^2/4c_0c_2$ which can be expressed in terms of skewness and kurtosis as

$$\kappa = \frac{c_1^2}{4c_0c_2} = \frac{S^2(K+3)^2}{4(4K-3S^2)(2K-3S^2-6)} \quad (4)$$

The range of parameter κ for $\kappa < 0$, $0 < \kappa < 1$ and $\kappa > 1$, characterise type I, type IV and type VI distributions, respectively. In this work, we are exploiting the statistics of the parameter κ for median filtering forensics. For detailed information about Pearson distributions and special cases of Pearson distributions, one may see [37, 39].

3.2 Motivation for new feature set construction

Sliding window median filter of the window size $s \times s$ ($s = 3, 5, 7, \dots$) introduces dependence or correlations among the neighbouring pixels of an image. The extent of dependence varies with the size of the window used and the distance between pixels. This effect is known as *streaking effect* and it is quantitatively analysed by Bovik [33]. In most of the previous work [6, 7, 11, 13, 32], these correlations are used to determine distinguishing statistical features for median filtering forensics. In these works, either pixel values [6, 10, 32], first-order pixel difference [11–13] or MFR [7, 8] of images is employed to extract detection features. While using image pixel values or first-order difference values, image edge information and JPEG compression blocking artefacts may obstruct capturing of median filtering traces. Kang *et al.* [7] and Li *et al.* [18] demonstrated the efficacy of residual-based features over pixel value based and first-order difference based features. MFR is defined as

$$I_{\text{MFR}}(i, j) = p(i, j) - \text{median}_s[p(i, j)] \quad (5)$$

where $I_{\text{MFR}}(i, j)$ denotes the MFR version of the pixel value $p(i, j)$ and $\text{median}_s[\cdot]$ denotes the median filtering operation within the neighbourhood of size $s \times s$. Due to the better performance of MFR based features for JPEG compressed images [7], MFR is exploited in our work to distinguish between original and median filtered images.

To determine the unique characteristics of median filtered image MFR, the image MFR is divided into sliding blocks of size 3×3 . Median filtering tends to reproduce already existing grey levels in a block which result in limited residual values in a residual block. Thus, the first-order statistics of the residual block is highly prone to be affected. Equation (4) shows that the parameter κ is a polynomial ratio of skewness (S) and kurtosis (K). Therefore, the parameter κ can provide insight information regarding residual block statistics. Capturing changes in first-order statistics of residual block by the parameter κ is the motivation for the novel feature set construction in the proposed work.

3.3 κ vector and κ vector histogram formation

In image MFRs, a block with single residual value (SRV) is referred to as SRV block. These SRV blocks have zero variance, resulting in undefined skewness and kurtosis values. As a result, the κ values of SRV blocks are also undefined. The undefined κ values for SRV blocks are denoted as κ_{SRV} . However, SRV blocks do not participate in the construction of the final κ vector, but the count of such blocks in an image is used as a feature in this work. It has been observed that the location of SRV blocks in original image MFR and median filtered image MFR does not coincide. Thus, to maintain equal lengths of original image MFR κ vector and median filtered image MFR κ vector, only the blocks which do not have κ_{SRV} in either of κ vectors have been considered.

The method adopted for κ vector generation is shown in Fig. 1. Figs. 1a and d represent the original image, 3×3 median filtered image and Figs. 1b and e represent corresponding MFRs. In Fig. 1,

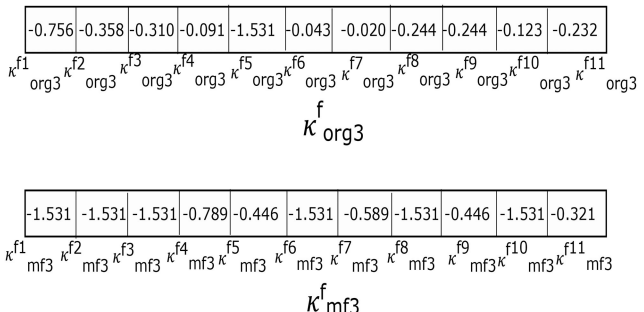


Fig. 2 Final κ vectors for original image MFR and 3×3 median filtered image MFR example blocks shown in Figs. 1c and f

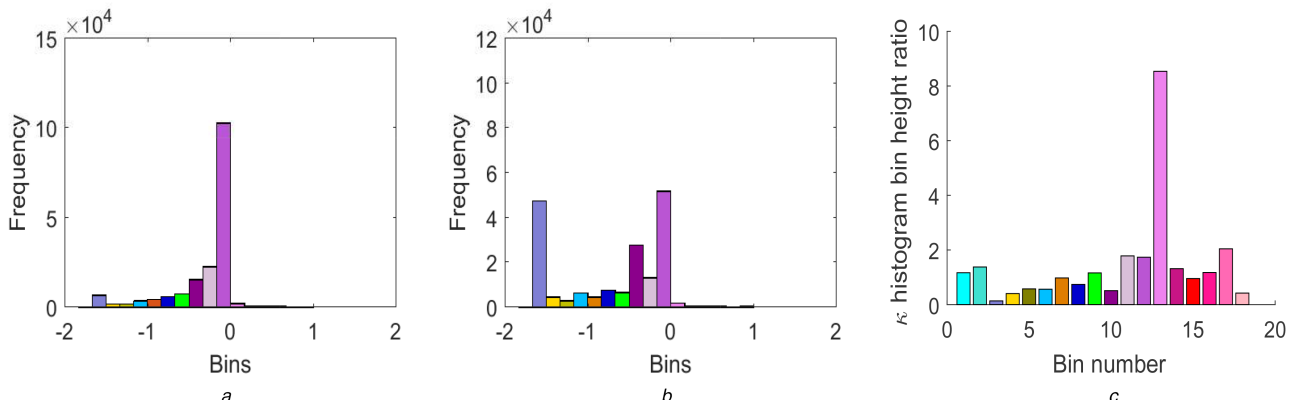


Fig. 3 Histogram comparison of κ^f_{org3} and κ^f_{mf3}

- (a) Original image MFR κ^f_{org3} histogram,
- (b) Median filtered image MFR (window size $s = 3$) κ^f_{mf3} histogram and,
- (c) Bar plot of the ratio of κ^f_{org3} histogram bin heights to κ^f_{mf3} histogram bin heights. The same colour codes represent corresponding 18 bins and bars in Figs. 3a–c

κ vectors construction from corresponding example blocks of size 6×6 (red marked blocks in Figs. 1b and e) from original image MFR (Fig. 1b) and 3×3 median filtered image MFR (Fig. 1e) have been demonstrated. For 6×6 sized example block, κ values for each of sliding blocks of size 3×3 has been determined and denoted as κ_{op}^i where $op \in \{org3, mf3\}$ and $i \in N$ where $N = \{n | n \in \mathbb{Z}^+ \& 1 \leq n \leq 16\}$. Here, $org3$ and $mf3$ denote blocks from original image MFR and median filtered image MFR with $s = 3$, respectively. The blue coloured block in Fig. 1c represents an SRV block in the original image MFR example block and computed κ_{SRV} is at ninth position in κ_{org3} vector. Corresponding ninth position in a κ_{mf3} vector in Fig. 1f is also filled with blue colour. The green coloured block in Fig. 1f represents one of the SRV blocks in 3×3 median filtered image MFR example block. Corresponding computed κ_{SRV} is at the third position in κ_{mf3} vector. Other SRV blocks in 3×3 median filtered image MFR example block result in κ_{mf3}^5 , κ_{mf3}^6 and κ_{mf3}^7 in κ_{mf3} and filled with green colour. Corresponding locations in κ_{org3} vector are also filled with green colour as shown in Fig. 1c. For the equal length of κ_{org3} and κ_{mf3} vectors, final κ vectors are determined by removing all green and blue coloured blocks (shown by red cross marks on green and blue colour filled blocks in Figs. 1c and f) from κ_{org3} and κ_{mf3} vectors. Resulting final vectors are termed as κ^f_{org3} and κ^f_{mf3} as shown in Fig. 2.

As discussed above, the κ_{org3} and κ_{mf3} for an original image MFR (Fig. 1b) and median filtered image MFR (Fig. 1e) are determined using the above method. Assuming B denotes the total number of sliding blocks in an image MFR such that $N = \{n | n \in \mathbb{Z}^+ \& 1 \leq n \leq B\}$ and $i \in N$. The locations of κ_{SRV} in either of κ_{org3} or κ_{mf3} can be extracted using

$$I = \{i | \kappa_{SRV} \in (\kappa_{org3}^i \cup \kappa_{mf3}^i)\} \quad (6)$$

Further, κ^f_{org3} and κ^f_{mf3} can be defined as

$$\kappa^f_{org3} = \{\kappa_{org3}^j | j \in (N \setminus I)\} \quad (7)$$

$$\kappa^f_{mf3} = \{\kappa_{mf3}^j | j \in (N \setminus I)\} \quad (8)$$

The histograms for resulting κ^f_{org3} , κ^f_{mf3} vectors and the ratio of κ^f_{org3} histogram bins height to κ^f_{mf3} histogram bins height in the form of the bar graph are plotted in Figs. 3a–c, respectively. The Doane [43] formula is used to determine the number of optimum bins for histograms. It should be noted that the magnitude of bars in Fig. 3c significantly deviates from unity value which shows significant changes in bins height of κ^f_{mf3} histogram as compared to the κ^f_{org3} histogram.

3.4 κ analysis of distinct residual value blocks in UCID database images

Streaking effect [33] is found to be responsible for the reduction in distinct residual values in a median filtered image MFR as compared to an original image MFR. To quantitatively analyse the streaking effect phenomenon, the original image MFR, median filtered ($s = 3$ and $s = 5$) images MFRs are divided into sliding blocks of size 3×3 . Further, distinct residual values ($N_R = 1, 2, 3, \dots, 9$) in every block have been counted and the percentage of such different distinct residual value blocks in original and median filtered ($s = 3, 5$) images MFRs have been determined. This method is followed for 1338 UCID [27] database images and average observations (in %) are reported in Table 1. From Table 1, it can be observed that a maximum number of residual blocks in an original image MFR corresponds to $N_R = 4$ whereas the maximum number of residual blocks in median filtered images ($s = 3$ and $s = 5$) MFRs correspond to $N_R = 2$ and $N_R = 1$, respectively. Thus, first-order statistics of each residual block will significantly change from original image MFR to median filtered images ($s = 3, 5$) MFRs. The changes in first-order block statistics have been captured in terms of κ value for each sliding residual

Table 1 Average percentage (%) of distinct residual value blocks in the UCID database original images MFR (ORG_IMG_MFR) and median filtered images ($s = 3$ and $s = 5$) MFRs (MF3_IMG_MFR and MF5_IMG_MFR)

N_R	Percentage (%) of distinct residual value blocks in		
	ORG_IMG_MFR	MF3_IMG_MFR	MF5_IMG_MFR
1	2.44	19.41	31.63
2	4.94	25.86	27.38
3	14.91	22.24	19.57
4	15.06	14.52	10.65
5	14.61	9.59	6.05
6	14.50	5.25	0.03
7	14.47	2.23	1.25
8	12.14	0.72	0.38
9	6.92	0.18	0.08

N_R denotes the count of distinct residual values in a block. Maximum contribution in each case is given in bold values.

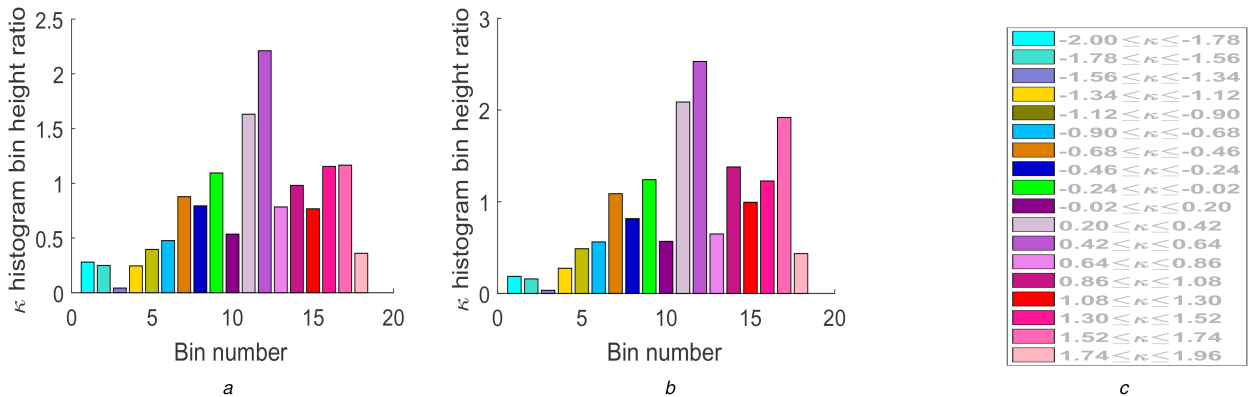


Fig. 4 Bar graph of the ratio of histogram bins (18 bins) average height for UCID [27] database 1338

- (a) Original images MFRs to corresponding 3×3 median filtered images MFRs,
- (b) Original images MFRs to corresponding 5×5 median filtered images MFRs and,
- (c) Common legend plot for Figs. 4a and b showing the κ range for different colour bars. The 18 bars of particular colours represent the same coloured bars in Fig. 3

block of image MFRs. Also, it can be observed from Table 1 that median filtered image MFR has a major share of 2–4 distinct residual value blocks which result in a complete redistribution of the histogram of $\kappa_{mf_3}^f$ concerning the histogram of $\kappa_{org_3}^f$ (Figs. 3a and b).

To make a generalisation from the above observations, a bar graph (Fig. 4a) of the ratio of $\kappa_{org_3}^f$ histogram bins average heights for 1338 original images MFRs to $\kappa_{mf_3}^f$ histogram bins average height of corresponding median filtered images MFRs is plotted. Similarly, a bar graph of the ratio of histogram bins average heights of 1338 original images MFRs to corresponding median filtered images MFRs with $s = 5$ is shown in Fig. 4b. These 1338 images are taken from UCID [27] database and are of similar size (384×512). Different colour bars in Figs. 4a and b correspond to the κ range shown in Fig. 4c. The bars in Figs. 4a and b show the variation of bins average height ratio from unity which support the observation deduced from Fig. 3c. It is interesting to note that for all 1338 images, $\sim 99\%$ of κ values in $\kappa_{org_3}^f$ and $\kappa_{mf_3}^f$ vectors lie within the range $[-2, 2]$. Thus, outliers from $\kappa_{org_3}^f$ and $\kappa_{mf_3}^f$ vectors are dropped and histograms are plotted for κ range $[-2, 2]$.

3.5 Novel feature set

Based on observations shown in Figs. 3 and 4, a novel feature set has been proposed for median filtering forensics. This comprises of 23 distinguishing features which are listed as follows.

3.5.1 κ histogram bin height: Given the observations drawn in the foregoing section, image MFR κ histogram bins height change significantly when an image is median filtered with window size $s \times s$ ($s = 3$ and $s = 5$). Therefore, κ histogram bins height can be utilised as intrinsic fingerprints for median filtering forensics. From Fig. 4, it has been observed that the ratio of $\kappa_{org_3}^f$ histogram bins

height to $\kappa_{mf_3}^f$ histogram bins height is significantly varied from unity which depicts complete redistribution of histogram bins height for median filtered image MFR as compared to original image MFR. Thus, the height of histogram bins from bin numbers 1 to 18 are considered as part of a proposed feature set and defined as

$$\text{HBH}_\kappa = [h_i] \quad 1 \leq i \leq 18 \quad \text{and} \quad i \in \mathbb{Z}^+ \quad (9)$$

where h_i denotes the height of the i th bin of κ vector histogram. MFR of the image under investigation is divided into 3×3 sliding blocks and κ value is calculated for each block. Total count of blocks after removal of SRV blocks is assumed to be N_b . If x_i and w_i are assumed as centre and width of the i th bin in κ vector histogram, h_i can be defined as

$$h_i = \sum_{j=1}^{N_b} \Psi(\kappa, x_i, w_i) \quad (10)$$

Here $\Psi(\kappa, x_i, w_i)$ can be defined as

$$\Psi(\kappa, x_i, w_i) = \begin{cases} 1 & \left(x_i - \frac{w_i}{2}\right) \leq \kappa \leq \left(x_i + \frac{w_i}{2}\right), \\ 0 & \text{otherwise.} \end{cases} \quad (11)$$

In (11), the κ range is similar to as shown in Fig. 4c.

3.5.2 Moments of block κ distribution: As observed from Fig. 4, κ values are redistributed due to median filtering operation and hence, the moments of the κ vector will give useful insight for median filtering detection. To this end, the ratio of the average value of moments (mean, variance, skewness and kurtosis) for

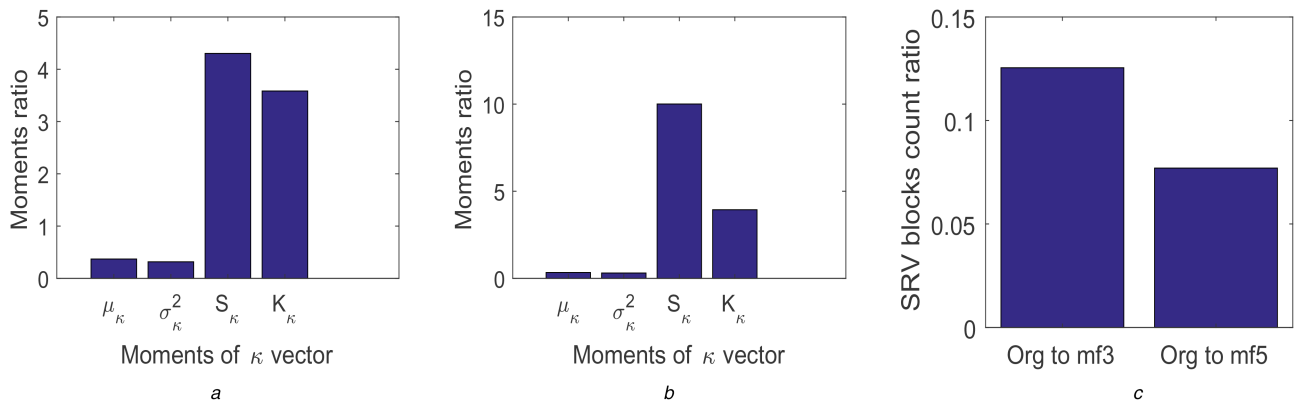


Fig. 5 Bar plots of the ratio of average of the first four moments of

(a) κ_{org3}^f and κ_{mf3}^f ,

(b) κ_{org5}^f and κ_{mf5}^f and,

(c) Ratio of the average of SRV block count for 1338 original, 3×3 median filtered and ratio of the average of SRV block count for 1338 original, 5×5 median filtered images MFRs. These images are taken from UCID [27] database

1338 original (UCID [27] database) images MFRs to 1338 corresponding median filtered images ($s = 3$ and $s = 5$) MFRs have been plotted in Figs. 5a and b, respectively. It has been observed from Fig. 5a that there is a significant change in the average value of moments of κ_{mf3}^f as compared to κ_{org3}^f , thus the ratios are different from unity. Similar observations can be made for moments of κ_{mf5}^f and κ_{org5}^f from Fig. 5b. Thus, four moments of κ vectors are considered as distinguishing features for median filtering forensics and are defined as

$$MOM_{\kappa} = [\mu_{\kappa}, \sigma_{\kappa}^2, S_{\kappa}, K_{\kappa}] \quad (12)$$

where μ_{κ} , σ_{κ}^2 , S_{κ} and K_{κ} denote mean, variance, skewness and kurtosis of the κ vector, respectively.

3.5.3 Count of SRV blocks: Fig. 5c shows the ratio of the average count of SRV blocks for MFRs of 1338 original to an average count of SRV blocks for MFRs of 1338 corresponding median filtered images (window size $s \times s$ for $s = 3, 5$). It may be noted from Fig. 5c that count of SRV blocks (C_{SRV}) tends to increase for median filtered images MFRs as compared to original images MFRs. Thus, C_{SRV} can be utilised as a distinguishing feature for median filtering forensics. For the k th residual block of size $\omega \times \omega$ with residual values $r_1^k, r_2^k, \dots, r_{\omega^2}^k$, the feature C_{SRV} can be defined as

$$C_{SRV} = \sum_{k=1}^B \Phi(r_p^k, r_q^k) \quad (13)$$

where B denotes the total number of sliding blocks in an image MFR and $\Phi(r_p^k, r_q^k)$ can be defined as

$$\Phi(r_p^k, r_q^k) = \begin{cases} 1 & r_p^k = r_q^k, \quad \forall p, q \\ 0 & \text{otherwise.} \end{cases} \quad (14)$$

3.5.4 Composite feature set: The proposed composite feature set (F_k^{23}) comprises 23 distinguishing features for median filtering forensics. Using (9), (12) and (13), F_k^{23} can be defined as

$$F_k^{23} = [HBH_{\kappa}, MOM_{\kappa}, C_{SRV}] \quad (15)$$

In this work, the obtained feature set F_k^{23} is compared against state-of-the-art detectors *MFF* [6], *AR* [7], *MFD* [10], *SK/SKR* [32]. The efficacy of feature set F_k^{23} along with *MFF*, *AR*, *MFD* and *SK/SKR* have been analysed by taking two-dimensional projections of feature sets using linear discriminant analysis (LDA). It can be

observed from Fig. 6 that the feature set F_k^{23} is capable of distinguishing between 384×512 sized original and the corresponding median filtered images under JPEG compression with quality factor $Q = 70$ with minimum overlap between three classes of classification. The feature sets F_k^{23} , *MFF*, *AR*, *MFD* and *SK/SKR* are generated for a combined database of 5352 images, created by randomly selected 1338 images from each of UCID [27], BOWS2 [28], BOSSBase [29] and RAISE [30] databases and centrally cropped to size 384×512 .

4 Experimental setup

In this section, the databases and methodology used to develop a generalised observation about the effectiveness of the proposed feature set F_k^{23} have been discussed. Similar databases and methods have been used in previous works [6–8, 11, 19, 32].

4.1 Image databases

In this work, five different databases, uncompressed colour image database (UCID) [27], BOWS2 [28], BOSSBase [29], raw image dataset (RAISE) [30] and NRCS [31], are used for comprehensive evaluation of the proposed detector F_k^{23} for the purpose of median filtering forensics. Various combinations of these databases are also used in previous works [6–8, 11, 19, 32]. Using these databases, the following three datasets are created for simulation of results:

- (i) Ω_{COM} : A combined database Ω_{COM} of 5352 images has been created by randomly selecting 1338 images from each of UCID [27], BOWS2 [28], BOSSBase [29] and RAISE [30] databases. All selected images are centrally cropped to size 384×512 and converted to grey-scale images.
- (ii) Ω_{NRCS} : NRCS [31] database is developed by United States Department of Agriculture. It includes various agricultural images under different categories. Ω_{NRCS} is created by randomly selecting 1309 .tif format images and centrally cropped to a fixed size of 384×512 .
- (iii) Ω_{CNN} : For a comparison of proposed detector performance against CNN-based detector [19], a large database of 13,985 images is created by selecting 10,000 images from BOSSBase [29] database, randomly selected 1338 images from each of BOWS2 [28], UCID [27] databases and randomly selected 1309 images from NRCS [31] database. All images in the set are centrally cropped to size 128×128 .

4.2 Training–testing pairs

To assess the benefits and limitations of the proposed feature vector F_k^{23} , following training–testing pairs are formed:

(i) Each of the above-discussed sets Ω_X where $X \in \{\text{COM}, \text{NRCS}, \text{CNN}\}$ is median filtered with window size $s \times s$ ($s = 3$ and $s = 5$) to create sets $\Omega_X^{\text{MF}_3}$ and $\Omega_X^{\text{MF}_5}$, respectively. To distinguish between original and median filtered images in uncompressed form, SVM is trained using $\{\Omega_{\text{COM}}(I), \Omega_{\text{COM}}^{\text{MF}_3}(I)\}$ and $\{\Omega_{\text{COM}}(I), \Omega_{\text{COM}}^{\text{MF}_5}(I)\}$, whereas testing is performed on the complementary set. To ensure the proposed detector's efficacy on unseen images, testing is also performed on randomly selected 500 images from $\{\Omega_{\text{NRCS}}, \Omega_{\text{NRCS}}^{\text{MF}_3}\}$ and 500 images from $\{\Omega_{\text{NRCS}}, \Omega_{\text{NRCS}}^{\text{MF}_5}\}$. For comparison of the proposed detector against CNN-based detector, 70% images from sets $\{\Omega_{\text{CNN}}, \Omega_{\text{CNN}}^{\text{MF}_3}\}$ and $\{\Omega_{\text{CNN}}, \Omega_{\text{CNN}}^{\text{MF}_5}\}$ are used for training and testing are performed on the remaining 30% images in the sets.

(ii) In order to determine the detector performance under JPEG compression, each of Ω_X , $\Omega_X^{\text{MF}_3}$ and $\Omega_X^{\text{MF}_5}$ is JPEG compressed with a quality factor Q , $Q \in \{90, 70, 50, 30\}$, to obtain sets $\Omega_X^{\text{ORG}+Q}$, $\Omega_X^{\text{MF}_3+Q}$ and $\Omega_X^{\text{MF}_5+Q}$, respectively. Training sets are formed as $\{\Omega_{\text{COM}}^{\text{ORG}+Q}(I), \Omega_{\text{COM}}^{\text{MF}_3+Q}(I)\}$ and $\{\Omega_{\text{COM}}^{\text{ORG}+Q}(I), \Omega_{\text{COM}}^{\text{MF}_5+Q}(I)\}$ while testing is performed on remaining images in the sets. To ensure the generalised behaviour of the proposed detector on unseen images, testing is also performed on randomly selected 500 images from $\{\Omega_{\text{NRCS}}^{\text{ORG}+Q}, \Omega_{\text{NRCS}}^{\text{MF}_3+Q}\}$ and 500 images from $\{\Omega_{\text{NRCS}}^{\text{ORG}+Q}, \Omega_{\text{NRCS}}^{\text{MF}_5+Q}\}$ sets. For the database Ω_{CNN} , 70% images from sets $\{\Omega_{\text{CNN}}^{\text{ORG}+Q}, \Omega_{\text{CNN}}^{\text{MF}_3+Q}\}$ and $\{\Omega_{\text{CNN}}^{\text{ORG}+Q}, \Omega_{\text{CNN}}^{\text{MF}_5+Q}\}$ are used for training and 30% images are used for testing purpose.

(iii) For detection of median filtering against average filtering, Gaussian filtering and rescaling operation, $\Omega_{\text{COM}}^{\text{AVG}}$, $\Omega_{\text{COM}}^{\text{GAU}}$, and $\Omega_{\text{COM}}^{\text{RES}}$ are formed. These sets are formed by average filtering Ω_{COM} images with window size 3×3 , Gaussian filtering with standard

deviation $\sigma = 0.5$ and up-scaling with a factor of 1.5 using bi-cubic interpolation method. Each of these is JPEG compressed with a quality factor $Q = 90$ to form $\Omega_{\text{COM}}^{\text{AVG}+Q}$, $\Omega_{\text{COM}}^{\text{GAU}+Q}$, and $\Omega_{\text{COM}}^{\text{RES}+Q}$. SVM is trained using $\{\Omega_{\text{COM}}^{\text{PROC}}(I), \Omega_{\text{COM}}^{\text{MF}_3}(I)\}$ and $\{\Omega_{\text{COM}}^{\text{PROC}}(I), \Omega_{\text{COM}}^{\text{MF}_5}(I)\}$, where $\text{PROC} \in \{\text{AVG}, \text{GAU}, \text{RES}\}$ and testing is performed on the complementary sets. To ensure median filtering detection against other similar manipulations in compressed form, SVM is trained using $\{\Omega_{\text{COM}}^{\text{PROC}+Q}(I), \Omega_{\text{COM}}^{\text{MF}_3+Q}(I)\}$ and testing is performed on the complementary sets.

(iv) To detect median filtering against different attacks, $\Omega_{\text{COM}}^{\text{MF}_35}$ is formed by combining 50% images from each of the median filtered image sets $\Omega_{\text{COM}}^{\text{MF}_3}$ and $\Omega_{\text{COM}}^{\text{MF}_5}$. $\Omega_{\text{COM}}^{\text{ALL}}$ is formed by combining 25% images from each of $\Omega_{\text{COM}}^{\text{AVG}}$, $\Omega_{\text{COM}}^{\text{GAU}}$, $\Omega_{\text{COM}}^{\text{RES}}$ and Ω_{COM} . Training is done using $\{\Omega_{\text{COM}}^{\text{MF}_35}(I), \Omega_{\text{COM}}^{\text{ALL}}(I)\}$ and testing is performed on the complementary set.

(v) To determine median filtering window size ($s = 3$ or $s = 5$), training is performed using $\{\Omega_{\text{COM}}^{\text{MF}_3}(I), \Omega_{\text{COM}}^{\text{MF}_5}(I)\}$ and $\{\Omega_{\text{COM}}^{\text{MF}_3+Q}(I), \Omega_{\text{COM}}^{\text{MF}_5+Q}(I)\}$ where $Q \in \{90, 70, 50, 30\}$. Testing is performed on the remaining images in the sets.

Above discussed training–testing pairs are also formed for image resolutions 256×256 and 128×128 , by cropping central part from original size images of Ω_{COM} and Ω_{NRCS} datasets. After that, all images are converted to grey-scale images before processing.

4.3 Experimental methodology

In this work, the proposed detector F_k^{23} is compared against hand-crafted features based state-of-the-art detectors *MF* [6], *AR* [7], *MFD* [10], *SK/SKR* [32] and CNN-based detector [19]. It should be

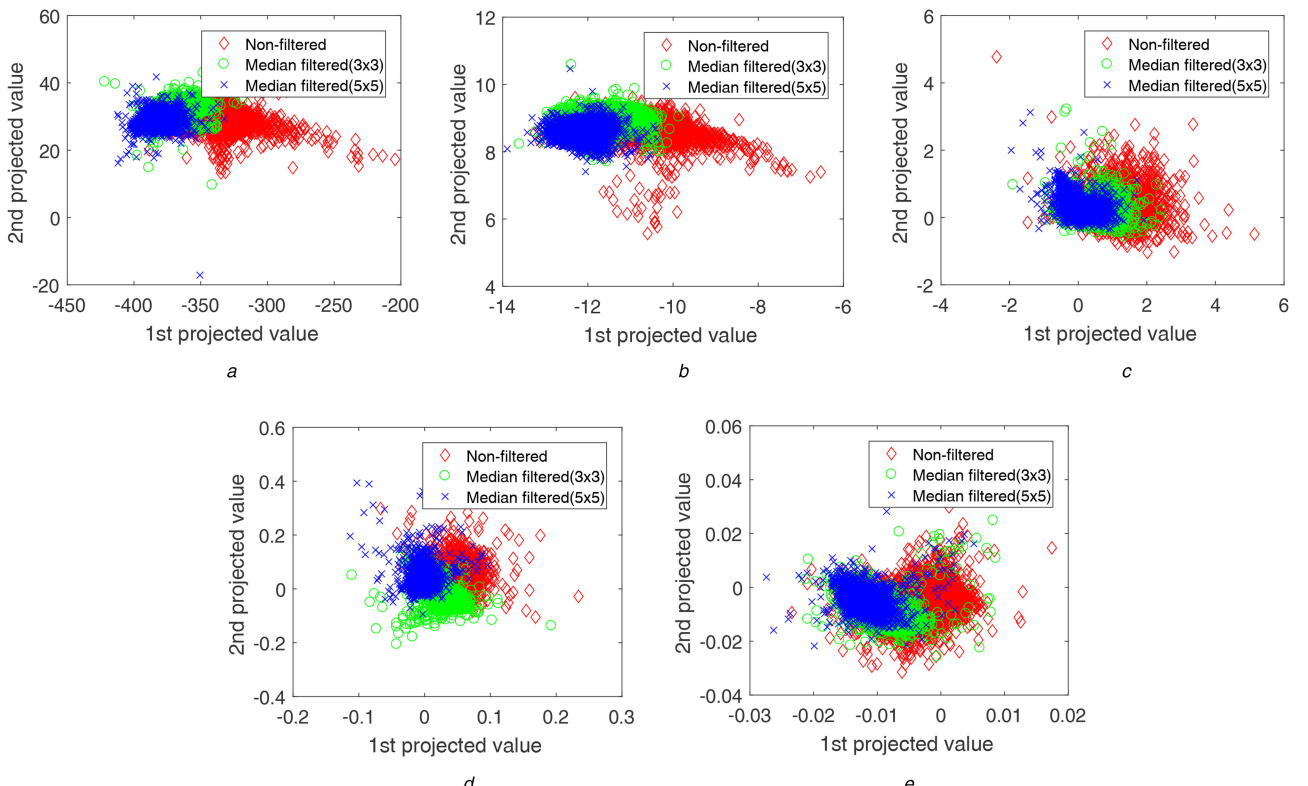


Fig. 6 Two-dimensional LDA projections of 384×512 sized original and corresponding median filtered images, all JPEG compressed with $Q = 70$, are shown for feature sets

- (a) F_k^{23} ,
- (b) SK/SKR ,
- (c) MFD ,
- (d) AR and,
- (e) MF

Table 2 Performance evaluation of proposed detector F_k^{23} using different kernel functions

S	Q	ORG + Q versus MF3 + Q					
		Quadratic		Cubic		Fine Gaussian	
		P_e	AUC	P_e	AUC	P_e	AUC
384 × 512	<i>UnC</i>	0.0010	0.9997	0.0012	0.9993	0.0020	0.9997
	90	0.0086	0.9958	0.0094	0.9940	0.0425	0.9915
	70	0.0211	0.9949	0.0223	0.9889	0.1226	0.9440
	50	0.0238	0.9943	0.0231	0.9878	0.1597	0.9139
	30	0.0262	0.9922	0.0283	0.9856	0.1816	0.8942
256 × 256	<i>UnC</i>	0.0014	0.9998	0.0014	0.9998	0.0036	0.9995
	90	0.0134	0.9967	0.2544	0.6709	0.0529	0.9877
	70	0.0296	0.9924	0.2585	0.7460	0.1410	0.9305
	50	0.0379	0.9894	0.2694	0.6555	0.1873	0.8895
	30	0.0386	0.9837	0.0448	0.9753	0.2161	0.8549
128 × 128	<i>UnC</i>	0.0020	0.9991	0.0026	0.9990	0.0054	0.9995
	90	0.0286	0.9899	0.0586	0.9761	0.0801	0.9727
	70	0.0559	0.9820	0.4219	0.5748	0.1646	0.9104
	50	0.0740	0.9726	0.3021	0.6359	0.2294	0.8454
	30	0.0827	0.9675	0.2899	0.7307	0.2451	0.8254

S and Q represent the image resolution and quality factor of compression, respectively. Best results are given in bold values.

noted that in [32], the feature set SK is proposed for uncompressed mode classification, whereas the feature set SK_R is proposed for compressed mode classification. Among hand-crafted features based detectors, performances of feature sets MFF , AR and MFD are determined using binary classifier $C\text{-}SVM$ with fine Gaussian kernel function whereas the performance of feature set SK/SK_R is reported using cubic kernel function. The classifier selection for prior art performance evaluation is based on classifiers used in original work.

Training and testing are performed using 4-fold cross-validation, i.e. 75% images are used for training and 25% images are used for testing. For the proposed feature set F_k^{23} , median filtering detection performances for training–testing pairs $\{\Omega_{COM}^{ORG+Q}, \Omega_{COM}^{MF3+Q}\}$ and $\{\Omega_{COM}^{ORG}, \Omega_{COM}^{MF3}\}$ are evaluated using $C\text{-}SVM$ with quadratic, cubic and fine Gaussian kernel functions and reported in Table 2. Here, S and Q denote image resolution and quality factor of compression, respectively. *UnC* denotes no-compression or uncompressed state. The proposed feature set achieves optimum performance by using quadratic kernel function. Thus, quadratic kernel function with 4-fold cross-validation is used for testing of proposed detector F_k^{23} .

For comparison against CNN-based detector, the performance of [19] is reported for 13,985 images of Ω_{CNN} using 70–30% holdout validation whereas proposed detector results are tabulated using binary classifier $C\text{-}SVM$ with quadratic kernel function and 70–30% holdout validation. The quadratic kernel function is given by

$$K(x_i, x_j) = (x_i^T \cdot x_j + 1)^2 \quad (16)$$

where x_i and x_j denote two different predictors for SVM classification.

5 Experimental results

The efficacy of the proposed feature set F_k^{23} is reported in terms of receiver operating characteristics (ROC) curves, the area under the ROC curve (AUC) and the minimum probability of error (P_e) of the classifier. The optimum operating point is obtained under the assumption of equal prior and equal costs, i.e.

$$P_e = \min \left(\frac{P_{fp} + P_{fn}}{2} \right) \quad (17)$$

where P_{fp} and P_{fn} denote the false positive and false negative rates, respectively.

5.1 Median Filtering Detection under no compression

Uncompressed median filtered images with window size $s \times s$ ($s = 3$ and $s = 5$) are detected against uncompressed original images and results are reported in Table 3 under the subheading $Q = UnC$. In this paper, *UnC* stands for detection in uncompressed mode. The results signify that the proposed detector F_k^{23} achieves almost perfect classification performance. The performance of the proposed detector F_k^{23} is found better than prior detectors MFF [6], AR [7], MFD [10] and SK [32] for image resolutions 384×512 , 256×256 and 128×128 . These results are reported for the dataset Ω_{COM} . Thus, under the uncompressed form, the proposed detector F_k^{23} is found to be robust irrespective of image types and resolutions.

5.2 Median filtering detection under post JPEG compression

JPEG compression, being widely used format for image storage, may be misused by a malicious user to hide the statistical fingerprints of median filtering. Therefore, the median filtering detector should be robust to distinguish median filtering in the presence of JPEG compression. In this paper, the proposed detector along with previous detectors is evaluated for median filtering detection under post JPEG compression. In this work, median filtering detection under compressed mode is denoted by ‘ $ORI + Q$ versus $MFs + Q$ ’ ($s = 3$ and $s = 5$), i.e. median filtering detection when both original and median filtered images are post JPEG compressed. To analyse the robustness of proposed detector F_k^{23} for median filtering detection in the compressed mode, results are simulated for database Ω_{COM} images for $Q \in \{90, 70, 50, 30\}$ and compared with the previous works (MFF [6], AR [7], MFD [10] and SK_R [32]). The results are reported in Table 3 which show that the proposed detector performs significantly better than state-of-art-methods under compressed state, especially for the combination of low-resolution (128×128) and post JPEG compression ($Q \in \{90, 70, 50, 30\}$).

The results obtained in Table 3 can be asserted using Fig. 6 which shows minimum overlap between two classes of classification (384×512 sized original and median filtered ($s = 3$) images, both compressed with quality factor $Q = 70$) using feature set F_k^{23} as compared to state-of-the-art detectors MFF [6], AR [7], MFD [10] and SK_R [32].

5.3 Cross-database performance evaluation

To evaluate the generalised performance of proposed detector and other existing detectors (MFF [6], AR [7], MFD [10] and SK/SK_R

Table 3 Classification results of post JPEG compressed median filtered images against post JPEG compressed original images-part 1

S	Q	ORI + Q versus MF3 + Q									
		F_k^{23}		SK/SKR		MFD		AR		MFF	
		P_e	AUC	P_e	AUC	P_e	AUC	P_e	AUC	P_e	AUC
384 × 512	UnC	0.0010	0.9997	0.0061	0.9972	0.2024	0.8730	0.0420	0.9913	0.0050	0.9997
	90	0.0086	0.9958	0.0114	0.9950	0.2703	0.8009	0.0351	0.9938	0.0951	0.9678
	70	0.0211	0.9949	0.0244	0.9888	0.3220	0.7513	0.0585	0.9797	0.1645	0.9161
	50	0.0238	0.9943	0.0042	0.9982	0.3381	0.7300	0.0952	0.9592	0.2082	0.8750
	30	0.0262	0.9922	0.0462	0.9799	0.3487	0.7136	0.1299	0.9284	0.2493	0.8340
256 × 256	UnC	0.0014	0.9998	0.0068	0.9967	0.1924	0.8761	0.0513	0.9864	0.0069	0.9993
	90	0.0134	0.9967	0.0111	0.9946	0.2417	0.8262	0.0384	0.9903	0.1046	0.9628
	70	0.0296	0.9924	0.0363	0.9825	0.2878	0.7863	0.0716	0.9709	0.1778	0.9061
	50	0.0379	0.9894	0.0082	0.9962	0.3172	0.7529	0.1050	0.9482	0.2205	0.8648
	30	0.0386	0.9837	0.0061	0.9975	0.3273	0.7324	0.1372	0.9210	0.2545	0.8317
128 × 128	UnC	0.0020	0.9991	0.0133	0.9946	0.1874	0.8880	0.0624	0.9793	0.0103	0.9990
	90	0.0286	0.9899	0.0274	0.9875	0.2276	0.8447	0.0600	0.9791	0.1229	0.9541
	70	0.0559	0.9820	0.1811	0.7909	0.2716	0.8016	0.0961	0.9530	0.1966	0.9859
	50	0.0740	0.9726	0.0924	0.9478	0.2941	0.7768	0.1150	0.9364	0.2408	0.8532
	30	0.0827	0.9675	0.1129	0.9321	0.3089	0.7568	0.1448	0.9127	0.2689	0.8248

Classification results of post JPEG compressed median filtered images against post JPEG compressed original images-part 2

S	Q	ORI + Q versus MF5 + Q									
		F_k^{23}		SK/SKR		MFD		AR		MFF	
		P_e	AUC	P_e	AUC	P_e	AUC	P_e	AUC	P_e	AUC
384 × 512	UnC	0.0010	0.9999	0.0021	0.9992	0.0839	0.9631	0.0160	0.9980	0.0036	0.9996
	90	0.0027	0.9986	0.0027	0.9981	0.1307	0.9342	0.0190	0.9982	0.0701	0.9811
	70	0.0067	0.9974	0.0077	0.9971	0.2183	0.8774	0.0246	0.9968	0.0937	0.9669
	50	0.0073	0.9987	0.0021	0.9984	0.2419	0.8487	0.0261	0.9968	0.1093	0.9592
	30	0.0096	0.9981	0.0098	0.9959	0.2467	0.8399	0.0297	0.9942	0.1256	0.9483
256 × 256	UnC	0.0014	0.9998	0.0032	0.9989	0.0831	0.9623	0.0183	0.9970	0.0052	0.9998
	90	0.0029	0.9997	0.0031	0.9982	0.1191	0.9356	0.0194	0.9975	0.0730	0.9791
	70	0.0081	0.9986	0.0102	0.9963	0.1921	0.8910	0.0334	0.9934	0.1011	0.9639
	50	0.0128	0.9981	0.0043	0.9987	0.2162	0.8694	0.0422	0.9895	0.1129	0.9554
	30	0.0174	0.9952	0.0027	0.9989	0.2255	0.8580	0.0524	0.9837	0.1371	0.9427
128 × 128	UnC	0.0023	0.9994	0.0060	0.9976	0.0842	0.9624	0.0242	0.9960	0.0097	0.9988
	90	0.0096	0.9979	0.0096	0.9971	0.1221	0.9368	0.0283	0.9959	0.0760	0.9760
	70	0.0183	0.9961	0.0188	0.9925	0.1791	0.8956	0.0505	0.9841	0.1083	0.9619
	50	0.0303	0.9927	0.0305	0.9882	0.1932	0.8834	0.0612	0.9790	0.1252	0.9502
	30	0.0348	0.9890	0.0359	0.9869	0.2013	0.8764	0.0735	0.9715	0.1477	0.9373

S and Q denote the size of images and quality factor of compression, respectively. The images are taken from the Ω_{COM} dataset.

Results for the proposed detector F_k^{23} are compared with MFF [6], AR [7], MFD [10] and SK/SKR [32] detectors. Best results are given in bold values.

[32]), testing is performed on completely unseen images. Corresponding classifiers (fine Gaussian SVM for MFF, AR, MFD, cubic SVM for SK/SKR and quadratic SVM for F_k^{23}) are trained using randomly selected 5352 images from the sets $\{\Omega_{\text{COM}}, \Omega_{\text{COM}}^{\text{MF}3}\}, \{\Omega_{\text{COM}}, \Omega_{\text{COM}}^{\text{MF}5}\}$ and testing is performed on randomly selected 500 images from the sets $\{\Omega_{\text{NRCS}}, \Omega_{\text{NRCS}}^{\text{MF}3}\}, \{\Omega_{\text{NRCS}}, \Omega_{\text{NRCS}}^{\text{MF}5}\}$, respectively. The results, in terms of P_e , for uncompressed mode detection are reported under the subheading UnC for different image resolutions in Table 4. To perform generalised ability test under post JPEG compression, randomly selected 5352 images from sets $\{\Omega_{\text{COM}}^{\text{ORG}+Q}, \Omega_{\text{COM}}^{\text{MF}3+Q}\}$ and $\{\Omega_{\text{COM}}^{\text{ORG}+Q}, \Omega_{\text{COM}}^{\text{MF}5+Q}\}$ are used to train corresponding classifiers. Testing is performed on randomly selected 500 images from sets $\{\Omega_{\text{NRCS}}^{\text{ORG}+Q}, \Omega_{\text{NRCS}}^{\text{MF}3+Q}\}$ and $\{\Omega_{\text{NRCS}}^{\text{ORG}+Q}, \Omega_{\text{NRCS}}^{\text{MF}5+Q}\}$. The results are reported in terms of P_e in Table 4. Table 4 reveals the efficacy of the proposed feature set F_k^{23} to classify cross-database median filtered images from original images in uncompressed and post JPEG compressed mode. In the uncompressed mode, the proposed feature set F_k^{23} performs perfect

classification with almost zero P_e for all resolution images. Also, F_k^{23} outperforms prior detectors in post JPEG compressed mode especially for low-resolution images compressed with low-quality factors, i.e. $Q = 30$.

5.4 Performance comparison against CNN-based detector

As compared to hand-crafted features-based detectors, CNN-based detectors efficiently extract low-level features from images. Thus, CNN-based detectors are found to be more robust to detect median filtering in small resolution images compressed with low-quality factors. However, CNN-based detectors require a large database and large training time. To ensure the efficacy of the proposed feature set F_k^{23} against CNN-based detector, F_k^{23} performance is compared against [19] and the results are reported in Table 5. To report concise results, the results are compiled only for small resolution images (128 × 128). Results in Table 5 show that the proposed detector completely outperforms CNN-based detector [19] in both uncompressed and compressed modes.

Table 4 Median filtering classification results, in terms of probability of error (P_e), on cross-database images

S	Q	Org + Q versus MF3 + Q					Org + Q versus MF5 + Q				
		F_k^{23}	SK/SK _R	MFD	AR	MFF	F_k^{23}	SK/SK _R	MFD	AR	MFF
384 × 512	UnC	0.0000	0.0060	0.1706	0.1081	0.0080	0.0019	0.0019	0.0643	0.0362	0.0175
	90	0.0181	0.0056	0.2631	0.2100	0.1866	0.0000	0.0019	0.1075	0.1149	0.1425
	70	0.0212	0.0261	0.3669	0.2534	0.2976	0.0040	0.0142	0.1916	0.1244	0.1963
	50	0.0378	0.4490	0.3544	0.2291	0.2738	0.0137	0.0361	0.2425	0.1489	0.2143
	30	0.0339	0.0959	0.3811	0.2707	0.3370	0.0120	0.0789	0.2367	0.1526	0.1998
256 × 256	UnC	0.0000	0.0220	0.1460	0.0998	0.0105	0.0000	0.0019	0.0418	0.0283	0.0099
	90	0.0480	0.0509	0.2382	0.1260	0.2408	0.0000	0.0040	0.0750	0.0887	0.1511
	70	0.0488	0.1752	0.3291	0.1674	0.2857	0.0019	0.0102	0.2142	0.0776	0.1955
	50	0.0400	0.2973	0.3481	0.1982	0.3146	0.0200	0.1153	0.2680	0.1080	0.1958
	30	0.0301	0.3683	0.3465	0.2281	0.3750	0.0267	0.0536	0.2448	0.1184	0.2158
128 × 128	UnC	0.0000	0.0225	0.1257	0.0972	0.0241	0.0000	0.0000	0.0412	0.0411	0.0185
	90	0.0361	0.0340	0.2175	0.1278	0.2392	0.0041	0.0021	0.0847	0.1051	0.1305
	70	0.0676	0.0520	0.2609	0.1265	0.2781	0.0118	0.0060	0.1933	0.0515	0.1804
	50	0.1031	0.0682	0.2785	0.1199	0.3023	0.0099	0.0213	0.2186	0.0598	0.1920
	30	0.0691	0.0997	0.3672	0.1620	0.3097	0.0235	0.0321	0.2062	0.0858	0.1850

S and Q represent the image resolution and quality factor of compression, respectively. Best results are given in bold values.

Table 5 Comparison of proposed detector F_k^{23} performance (P_e) against CNN-based detector [19]

Q	Org + Q versus MF3 + Q			Org + Q versus MF5 + Q		
	F_k^{23}	[19]	F_k^{23}	[19]		
UnC	0.0004	0.0032	0.0008	0.0057		
90	0.0223	0.0871	0.0058	0.0250		
70	0.0509	0.0858	0.0168	0.0422		
50	0.0683	0.1110	0.0247	0.1013		
30	0.0789	0.2372	0.0292	0.0602		

Q denotes the quality factor of compression. Best results are given in bold values.

Table 6 Classification results for median filtering window size for Ω_{COM} images

S	Q	MF3 + Q versus MF5 + Q									
		F_k^{23}		SK/SK _R		MFD		AR		MFF	
		P_e	AUC	P_e	AUC	P_e	AUC	P_e	AUC	P_e	AUC
384 × 512	UnC	0.0025	0.9996	0.0163	0.9917	0.1745	0.8826	0.0196	0.9988	0.0546	0.9860
	90	0.0026	0.9984	0.0047	0.9977	0.2346	0.8224	0.0211	0.9985	0.2218	0.8700
	70	0.0093	0.9979	0.0122	0.9948	0.3383	0.7160	0.0361	0.9929	0.2222	0.8665
	50	0.0107	0.9974	0.0131	0.9942	0.3538	0.7039	0.0499	0.9869	0.2305	0.8610
	30	0.0130	0.9973	0.0157	0.9942	0.3323	0.7293	0.0726	0.9745	0.2432	0.8466
256 × 256	UnC	0.0046	0.9983	0.0157	0.9915	0.1684	0.8954	0.0183	0.9983	0.0618	0.9828
	90	0.0050	0.9978	0.0055	0.9970	0.2219	0.8363	0.0290	0.9963	0.2269	0.8585
	70	0.0133	0.9970	0.0186	0.9918	0.3212	0.7382	0.0549	0.9847	0.2363	0.8527
	50	0.0190	0.9951	0.0204	0.9903	0.3310	0.7295	0.0662	0.9766	0.2418	0.8484
	30	0.0192	0.9942	0.0263	0.9885	0.3156	0.7497	0.0935	0.9586	0.2642	0.8283
128 × 128	UnC	0.0076	0.9975	0.0359	0.9854	0.1582	0.9080	0.0360	0.9939	0.0917	0.9693
	90	0.0117	0.9971	0.0131	0.9935	0.2099	0.8608	0.0447	0.9880	0.2462	0.8336
	70	0.0268	0.9932	0.0302	0.9863	0.3001	0.7694	0.0803	0.9649	0.2455	0.8414
	50	0.0327	0.9918	0.0411	0.9805	0.2963	0.7681	0.0959	0.9548	0.2512	0.8380
	30	0.0426	0.9878	0.0493	0.9774	0.2806	0.7905	0.1297	0.9284	0.2821	0.8100

S and Q denote the image resolution and quality factor of compression, respectively. Best results are given in bold values.

5.5 Median filtering window size detection

To extract the complete information about the processing history of an image, the forensic investigator should know the window size used to median filter the image. Thus, classification results for window size ($s = 3$ and $s = 5$) under uncompressed state (MF3 versus MF5) and under JPEG compression (MF3 + Q versus MF5 + Q) for $Q = 90, 70, 50$ and 30 are determined. These results are shown in Table 6 for different resolution images from the Ω_{COM} dataset. Classification results for F_k^{23} are compared with previous detectors (MFF [6], AR [7], MFD [10] and SK/SK_R [32]) and

reveal that the proposed detector F_k^{23} can effectively distinguish between $s = 3$ or $s = 5$ with the lowest probability of error (P_e) and the highest AUC amongst state-of-the-art detectors.

5.6 Median filtering detection against other manipulations

Many image processing operations such as average filtering (AVG), Gaussian filtering (GAU) and rescaling (RES) left similar statistical fingerprints on images such as median filtering does. The forensic analyser should verify that the image in question is actually median filtered or any similar operation is performed on it.

Table 7 Classification results for median filtering detection against various manipulations (AVG, GAU, RES) for different resolution (S) images of Ω_{COM}

S	F_k^{23}	MF3 versus			MF5 versus			MF35
		Avg	GAU	RES	Avg	GAU	RES	All
384 × 512	F_k^{23}	P_e	0.0088	0.0004	0.0009	0.0014	0.0007	0.0009
		AUC	0.9986	0.9998	1.0000	0.9996	0.9996	0.9996
	SK	P_e	0.0089	0.0031	0.0034	0.0033	0.0018	0.0016
		AUC	0.9962	0.9990	0.9984	0.9979	0.9994	0.9960
	MFD	P_e	0.0441	0.2152	0.1958	0.0375	0.0898	0.0851
		AUC	0.9918	0.8598	0.8917	0.9945	0.9592	0.9195
	AR	P_e	0.0346	0.0372	0.0423	0.0159	0.0153	0.0111
		AUC	0.9940	0.9927	0.9908	0.9983	0.9985	0.9917
	MFF	P_e	0.0181	0.0046	0.0038	0.0162	0.0039	0.0029
		AUC	0.9985	0.9998	0.9997	0.9984	0.9996	0.9998
256 × 256	F_k^{23}	P_e	0.0108	0.0011	0.0022	0.0018	0.0017	0.0021
		AUC	0.9984	1.0000	0.9983	0.9996	1.0000	0.9995
	SK	P_e	0.0066	0.0059	0.0048	0.0028	0.0021	0.0029
		AUC	0.9966	0.9976	0.9981	0.9989	0.9991	0.9984
	MFD	P_e	0.0507	0.2086	0.1880	0.0453	0.0887	0.0882
		AUC	0.9887	0.8712	0.8986	0.9931	0.9600	0.9638
	AR	P_e	0.0380	0.0463	0.0550	0.0237	0.0160	0.0167
		AUC	0.9918	0.9876	0.9829	0.9969	0.9983	0.9858
	MFF	P_e	0.0213	0.0072	0.0068	0.0213	0.0056	0.0055
		AUC	0.9984	0.9994	0.9994	0.9977	0.9995	0.9985
128 × 128	F_k^{23}	P_e	0.0191	0.0025	0.0042	0.0030	0.0023	0.0036
		AUC	0.9972	0.9996	0.9990	0.9987	0.9994	0.9992
	SK	P_e	0.0100	0.0082	0.0074	0.0033	0.0037	0.0043
		AUC	0.9974	0.9962	0.9974	0.9980	0.9987	0.9984
	MFD	P_e	0.0636	0.1960	0.1750	0.0502	0.0909	0.0865
		AUC	0.9854	0.8853	0.9136	0.9908	0.9607	0.9651
	AR	P_e	0.0602	0.0649	0.0838	0.0392	0.0240	0.0168
		AUC	0.9812	0.9806	0.9648	0.9906	0.9966	0.9984
	MFF	P_e	0.0177	0.0107	0.0092	0.0211	0.0102	0.0085
		AUC	0.9986	0.9991	0.9992	0.9978	0.9988	0.9991

Best results are given in bold values.

To ensure median filtering operation, the median filtering detector should be able to distinguish between median filtering and other similar manipulations (AVG, GAU and RES). Thus, the proposed detector F_k^{23} along with MFF [6], AR [7], MFD [10] and SK/SK_R [32] are tested for median filtering detection against AVG, GAU, up-scaling and results are reported in Table 7. These results are simulated for uncompressed state images of the Ω_{COM} dataset. This classification problem consists of two classes, i.e. PROC and MFs and is denoted by ‘PROC versus MFs’ where $\text{PROC} \in \{\text{AVG}, \text{GAU}, \text{RES}\}$ and $s = 3, 5$. Also, the results are compiled for the training–testing pair $\{\Omega_{\text{COM}}^{\text{MF35}}, \Omega_{\text{COM}}^{\text{ALL}}\}$.

Furthermore, classification performance is determined when images are compressed with a quality factor $Q = 90$, i.e. ‘PROC + j90 versus MFs + j90’. Results for the case ‘PROC + j90 versus MFs + j90’ are shown in Fig. 7. Results in Table 7 and Fig. 7 signify that the proposed detector F_k^{23} can classify median filtering operation from a pool of similar manipulations with very less probability of error P_e and high AUC as compared to existing detectors.

6 Conclusion

This paper contributes a novel approach to the emerging field of median filtering forensics in images. The proposed scheme has employed first-order statistics of Pearson parameter κ for median filtering forensics. A 23-dimensional novel feature set, F_k^{23} , has been proposed based on distinct residual value blocks κ statistics in original and median filtered images MFRs. The proposed feature

vector F_k^{23} has been exhaustively tested for its efficacy against state-of-the-art methods. Detector F_k^{23} achieves a minimum probability of error and largest AUC in most of the test case scenarios as compared to existing hand-crafted features based detectors (MFF [6], AR [7], MFD [10] and SK/SK_R [32]) and CNN-based detector [19]. Generalisation ability tests are also conducted to ascertain the robustness of the proposed detector for cross-database images. The results clearly show that the proposed detector F_k^{23} achieves nearly perfect classification results for images of different resolutions under the uncompressed state. For median filtering detection under post JPEG compression, detection results (Tables 3–5) show that the proposed detector F_k^{23} exhibits significant improvement over existing hand-crafted features-based detectors and CNN-based detector for low-resolution images compressed with low-quality factors ($Q = 30$). Additionally, the proposed detector F_k^{23} is proved to be robust for window size detection and differentiating other manipulations from median filtering (Tables 6, 7 and Fig. 7). Thus, it may be concluded that the proposed detector is robust to detect global median filtering in all relevant test case scenarios.

7 Acknowledgment

The authors thank Dr. H.D. Yuan at Zhengzhou Information Science and Technology Institute, Zhengzhou and Dr. X. Kang at School of Information Science and Technology, Sun Yat-Sen University, Guangzhou for providing feature extraction code for MFF [6] and AR [7] schemes, respectively.

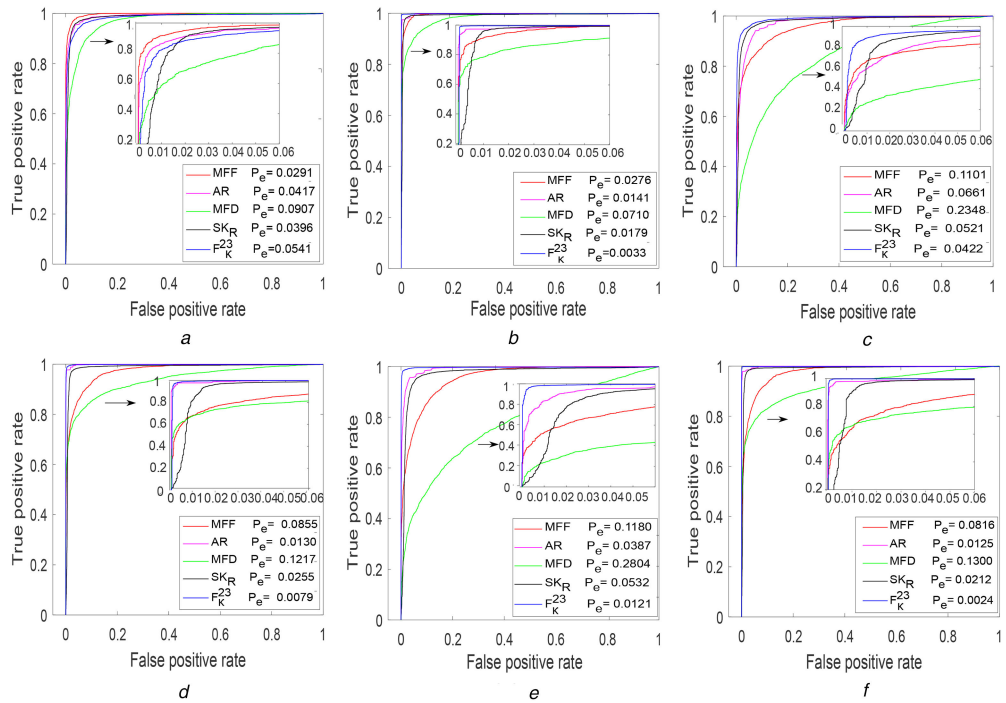


Fig. 7 Classification results in terms of ROC curves for training testing pairs

- (a) AVG + j90 versus MF3 + j90,
- (b) AVG + j90 versus MF5 + j90,
- (c) RES + j90 versus MF3 + j90,
- (d) RES + j90 versus MF5 + j90,
- (e) GAU + j90 versus MF3 + j90,
- (f) GAU + j90 versus MF5 + j90. Proposed detector results are compared with MFF [6], AR [7], MFD [10] and SK/SK_R [32] schemes. These results are shown for 384 × 512 sized 5352 images from the Ω_{COM} dataset

8 References

- [1] Popescu, A.C.: ‘Statistical tools for digital image forensics’ (Dartmouth College, Hanover, New Hampshire, 2004)
- [2] Popescu, A.C., Farid, H.: ‘Exposing digital forgeries by detecting traces of resampling’, *IEEE Trans. Signal Process.*, 2005, **53**, (2), pp. 758–767
- [3] Thai, T.H., Cogranne, R., Reitman, F., et al.: ‘Jpeg quantization step estimation and its applications to digital image forensics’, *IEEE Trans. Inf. Forensics Sec.*, 2017, **12**, (1), pp. 123–133
- [4] Stamm, M.C., Liu, K.J.R.: ‘Forensic detection of image manipulation using statistical intrinsic fingerprints’, *IEEE Trans. Inf. Forensics Sec.*, 2010, **5**, (3), pp. 492–506
- [5] Cao, G., Zhao, Y., Ni, R., et al.: ‘Contrast enhancement-based forensics in digital images’, *IEEE Trans. Inf. Forensics Sec.*, 2014, **9**, (3), pp. 515–525
- [6] Yuan, H.D.: ‘Blind forensics of median filtering in digital images’, *IEEE Trans. Inf. Forensics Sec.*, 2011, **6**, (4), pp. 1335–1345
- [7] Kang, X., Stamm, M.C., Peng, A., et al.: ‘Robust median filtering forensics using an autoregressive model’, *IEEE Trans. Inf. Forensics Sec.*, 2013, **8**, (9), pp. 1456–1468
- [8] Yang, J., Ren, H., Zhu, G., et al.: ‘Detecting median filtering via two-dimensional ar models of multiple filtered residuals’, *Multimedia Tools Appl.*, 2018, **77**, (7), pp. 7931–7953. Available at <http://dx.doi.org/10.1007/s11042-017-4691-0>
- [9] Shen, Z., Ni, J., Chen, C.: ‘Blind detection of median filtering using linear and nonlinear descriptors’, *Multimedia Tools Appl.*, 2016, **75**, (4), pp. 2327–2346. Available at <http://dx.doi.org/10.1007/s11042-014-2407-2>
- [10] Rhee, K.H.: ‘Median filtering detection using variation of neighboring line pairs for image forensics’, *J. Electron. Imaging*, 2016, **25**, (5), p. 053039. Available at <http://dx.doi.org/10.1117/1.JEI.25.053039>
- [11] Chen, C., Ni, J., Huang, J.: ‘Blind detection of median filtering in digital images: A difference domain based approach’, *IEEE Trans. Image Process.*, 2013, **22**, (12), pp. 4699–4710
- [12] Cao, G., Zhao, Y., Ni, R., et al.: ‘Forensic detection of median filtering in digital images’. Proc. IEEE Int. Conf. Multimedia and EXPO, Suntec city, Singapore, 2010, pp. 89–94
- [13] Kirchner, M., Fridrich, J.: ‘On detection of median filtering in digital images’. Proc. SPIE Media Forensics and Security II, San Jose, California, 2010, vol. 7541, pp. 754110–754110–12. Available at <http://dx.doi.org/10.1117/12.839100>
- [14] Niu, Y., Zhao, Y., Ni, R.: ‘Robust median filtering detection based on local difference descriptor’, *Signal Process., Image Commun.*, 2017, **53**, pp. 65–72. Available at <https://doi.org/10.1016/j.image.2017.01.008>
- [15] Liu, A., Zhao, Z., Zhang, C., et al.: ‘Median filtering forensics in digital images based on frequency-domain features’, *Multimedia Tools Appl.*, 2017, **76**, (21), pp. 22119–22132. Available at <https://doi.org/10.1007/s11042-017-4845-0>
- [16] Zhang, Y., Li, S., Wang, S., et al.: ‘Revealing the traces of median filtering using high-order local ternary patterns’, *IEEE Signal Process. Lett.*, 2014, **21**, (3), pp. 275–279. Available at <https://doi.org/10.1109/LSP.2013.2295858>
- [17] Wang, D.P., Gao, T., Yang, F.: ‘A forensic algorithm against median filtering based on coefficients of image blocks in frequency domain’, *Multimedia Tools Appl.*, 2018, **77**, (18), pp. 23411–23427. Available at <https://doi.org/10.1007/s11042-018-5651-z>
- [18] Li, H., Luo, W., Qiu, X., et al.: ‘Identification of various image operations using residual-based features’, *IEEE Trans. Circuits Syst. Video Technol.*, 2018, **28**, (1), pp. 31–45. Available at <https://doi.org/10.1109/TCSVT.2016.2599849>
- [19] Chen, J., Kang, X., Liu, Y., et al.: ‘Median filtering forensics based on convolutional neural networks’, *IEEE Signal Process. Lett.*, 2015, **22**, pp. 1849–1853
- [20] Tang, H., Ni, R., Zhao, Y., et al.: ‘Median filtering detection of small-size image based on cnn’, *J. Vis. Commun. Image Represent.*, 2018, **51**, pp. 162–168. Available at <http://www.sciencedirect.com/science/article/pii/S104732031830018X>
- [21] Bayar, B., Stamm, M.C.: ‘Constrained convolutional neural networks: A new approach towards general purpose image manipulation detection’, *IEEE Trans. Inf. Forensics Sec.*, 2018, **13**, pp. 2691–2706
- [22] Chen, B., Li, H., Luo, W.: ‘Image processing operations identification via convolutional neural network’, CoRR, 2017, abs/1709.02908. Available at <http://arxiv.org/abs/1709.02908>
- [23] Fan, W., Wang, K., Cayre, F., et al.: ‘Median filtered image quality enhancement and anti-forensics via variational deconvolution’, *IEEE Trans. Inf. Forensics Sec.*, 2015, **10**, (5), pp. 1076–1091
- [24] Sharma, S., Subramanyam, A.V., Jain, M., et al.: ‘Antiforensic technique for median filtering using L1-L2 TV model’. IEEE Int. Workshop on Information Forensics and Security WIFS, Abu Dhabi, United Arab Emirates, 2016, pp. 1–6. Available at <https://doi.org/10.1109/WIFS.2016.7823571>
- [25] Kirchner, M., Bohme, R.: ‘Hiding traces of resampling in digital images’, *Trans. Inf. Forensics Sec.*, 2008, **3**, (4), pp. 582–592. Available at <http://dx.doi.org/10.1109/TIFS.2008.2008214>
- [26] Stamm, M.C., Liu, K.J.R.: ‘Anti-forensics of digital image compression’, *Trans. Inf. Forensics Sec.*, 2011, **6**, (3), pp. 1050–1065. Available at <http://dx.doi.org/10.1109/TIFS.2011.2119314>
- [27] Schaeffer, G., Stich, M.: ‘Ucid: an uncompressed color image database’. Proc. SPIE, San Jose, California, 2003, vol. 5307, pp. 472–480. Available at <http://dx.doi.org/10.1117/12.525375>
- [28] Bas, P., Furon, T.: ‘Bows-2’, 2007
- [29] Bas, P., Filler, T., Pevný, T.: ‘Break our steganographic system: The ins and outs of organizing boss’. Information Hiding: 13th Int. Conf., IH 2011, Prague, Czech Republic, 18–20 May 2011, Revised Selected Papers, Berlin, Heidelberg, 2011, pp. 59–70. Available at http://dx.doi.org/10.1007/978-3-642-24178-9_5

- [30] Dang Nguyen, D.T., Pasquini, C., Conotter, V., *et al.* ‘A raw images dataset for digital image forensics’. Proc. of the 6th ACM Multimedia Systems Conf. (MMSys ‘15), Portland, Oregon, 2015, pp. 219–224. Available at <http://doi.acm.org/10.1145/2713168.2713194>
- [31] NRCS, U: ‘Natural resources conservation service photo gallery’, United States department of agriculture’, 2014. Available at <http://plants.usda.gov/>
- [32] Gupta, A., Singhal, D.: ‘Analytical global median filtering forensics based on moment histograms’, *ACM Trans. Multimed. Comput. Commun. Appl.*, 2018, **14**, (2), pp. 44:1–44:23
- [33] Bovik, A.C.: ‘Streaking in median filtered images’, *IEEE Trans. Acoust. Speech Signal Process.*, 1987, **35**, (4), pp. 493–503
- [34] Pevný, T., Bas, P., Fridrich, J.: ‘Steganalysis by subtractive pixel adjacency matrix’, *IEEE Trans. Inf. Forensics Sec.*, 2010, **5**, (2), pp. 215–224
- [35] Elderton, W.P., Johnson, N.L.: ‘Systems of frequency curves’ (Cambridge University Press, London, UK, 1969)
- [36] Nie, H., Chen, S.: ‘Lognormal sum approximation with type iv Pearson distribution’, *IEEE Commun. Lett.*, 2007, **11**, (10), pp. 790–792
- [37] Zhang, Q.T., Song, S.H.: ‘A systematic procedure for accurately approximating lognormal-sum distributions’, *IEEE Trans. Veh. Technol.*, 2008, **57**, (1), pp. 663–666
- [38] Renzo, M.D., Graziosi, F., Santucci, F.: ‘Approximating the linear combination of log-normal rvs via Pearson type iv distribution for uwb performance analysis’, *IEEE Trans. Commun.*, 2009, **57**, (2), pp. 388–403
- [39] Gupta, A., Karmeshu, : ‘Efficacy of Pearson distributions for characterization of gray levels in clinical ultrasound kidney images’, *Signal Image Video Process.*, 2015, **9**, (6), pp. 1317–1334
- [40] Gupta, A., Karmeshu, D.: ‘Statistical characterisation of speckle in clinical echocardiographic images with Pearson family of distributions’, *Def. Sci. J.*, 2011, **61**, (5), pp. 473–478. Available at <http://publications.drdo.gov.in/ojs/index.php/dsj/article/view/1163>
- [41] Delignon, Y., Pieczynski, W.: ‘Modeling non-Rayleigh speckle distribution in sar images’, *IEEE Trans. Geosci. Remote Sens.*, 2002, **40**, (6), pp. 1430–1435
- [42] Ketchantang, W., Derrode, S., Martin, L., *et al.*: ‘Pearson-based mixture model for color object tracking’, *Mach. Vis. Appl.*, 2008, **19**, (5), pp. 457–466. Available at <https://doi.org/10.1007/s00138-008-0124-4>
- [43] Doane, D.P.: ‘Aesthetic frequency classifications’, *Am. Stat.*, 1976, **30**, (4), pp. 181–183. Available at <http://amstat.tandfonline.com/doi/abs/10.1080/00031305.1976.10479172>